5-9-2017

Single-crystal Ih Ice Surfaces Unveil Connection between Macroscopic and Molecular Structure

Alexandra Brumberg
Tufts University

Kevin Hammonds
Montana State University, Bozeman

Ian Baker
Dartmouth College

Ellen H.G Backus
Max Planck Institute for Polymer Research

Patrick J. Bisson
Tufts University

See next page for additional authors

Single-crystal I_h ice surfaces unveil connection between macroscopic and molecular structure

Alexandra Brumberg[a], Kevin Hammonds[b], Ian Baker[c], Ellen H. G. Backus[d], Patrick J. Bisson[a], Mischa Bonn[d], Charles P. Daghlian[e], Markus Mezger[d,f], and Mary Jane Shultz[a,1]

[a]Department of Chemistry, Laboratory for Water and Surface Studies, Tufts University, Medford, MA 02155; [b]Department of Civil Engineering, Montana State University, Bozeman, MT 59717; [c]Thayer School of Engineering, Dartmouth College, Hanover, NH 03755; [d]Department of Molecular Spectroscopy, Max Planck Institute for Polymer Research, 55128 Mainz, Germany; [e]Electron Microscope Facility, Dartmouth College, Hanover, NH 03755; and [f]Institute of Physics, Johannes Gutenberg University Mainz, 55128 Mainz, Germany

Edited by Peter J. Rossky, Rice University, Houston, TX, and approved April 17, 2017 (received for review February 22, 2017)

Physics and chemistry of ice surfaces are not only of fundamental interest but also have important impacts on biological and environmental processes. As ice surfaces—particularly the two prism faces—come under greater scrutiny, it is increasingly important to connect the macroscopic faces with the molecular-level structure. The microscopic structure of the ubiquitous ice I_h crystal is well-known. It consists of stacked layers of chair-form hexagonal rings referred to as molecular hexagons. Crystallographic unit cells can be assembled into a regular right hexagonal prism. The bases are labeled crystallographic hexagons. The two hexagons are rotated 30° with respect to each other. The linkage between the familiar macroscopic shape of hexagonal snowflakes and either hexagon is not obvious per se. This report presents experimental data directly connecting the macroscopic shape of ice crystals and the microscopic hexagons. Large ice single crystals were used to fabricate samples with the basal, primary prism, or secondary prism faces exposed at the surface. In each case, the same sample was used to capture both a macroscopic etch pit image and an electron backscatter diffraction (EBSD) orientation density function (ODF) plot. Direct comparison of the etch pit image and the ODF plot compellingly connects the macroscopic etch pit hexagonal profile to the crystallographic hexagon. The most stable face at the ice–water interface is the smallest area face at the ice–vapor interface. A model based on the molecular structure of the prism faces accounts for this switch.

ice | molecular structure | etching | EBSD | statistical model

At atmospheric pressure, ice grows as hexagonal prisms (Fig. 1), familiar as the six-sided shape of a snowflake. Even before atoms were known, Kepler (1611) (1) speculated about the connection between the sixfold symmetry and the underlying microscopic structure. Experimental evidence for the molecular connection rests on assuming low crystallographic indices for hoarfrost dendrites (2) and Tyndall flowers (3, 4). However, it is now known that, for all solids—including ice—the fundamental connection between macroscopic shape and molecular configuration is in the surface energy of the various faces; i.e., Wulff (5–8) construction indicates that the lowest energy face has the largest exposed surface area. Thermal conduction and molecular transport can modify the equilibrium structure, capturing a kinetically controlled shape. For ice, kinetic growth experiments (9–11) show that surface energies are closely matched and thus, easily affect the observed shape. Furthermore, mechanical stress strongly impacts the shape of inclusions (12), raising the potential for the molecular structure–stress connection clouding the structure–hexagonal shape connection. Hence, the assumption that the primary prism face—the rectangular sides of hoarfrost dendrites, Tyndall flowers, or snowflakes—coincides with the crystallographic $\{10\bar{1}0\}$ face is not a priori supported. This work avoids stress and dendrite issues by using large, optically perfect single crystals, hence clearly connecting macroscopic shapes with molecular-level structure. Importantly, the correlation supports a molecular-level entropy connection with observed growth at the liquid–solid interface.

The connection between the macroscopic shape and the molecular-level configuration is becoming increasingly important as attention shifts to the molecular-level chemical and physical phenomena occurring at different crystallographic faces—specifically the prismatic faces. Recent work with nanoparticle growth (6–8) has shown that dangling bond, nearest neighbor, and next nearest neighbor configurations determine face energy: a clear demonstration of how the molecular configuration connects to macroscopic properties.

On the molecular level, hexagonal ice contains two types of regular right hexagonal prisms (Fig. 2): a molecular prism related to stacks of water molecules arranged in chair hexagonal rings and a crystallographic prism made of three unit cells of the rhombohedral Bravais lattice. The rectangular sides of these two prisms have quite distinct dangling bonds and neighbor configurations. Rectangular sides of molecular hexagonal prisms consist of chains of hydrogen-bonded water molecules and lack a bilayer structure. In contrast, rectangular sides of crystallographic hexagonal prisms consist of pairs of hydrogen-bonded water molecules in the top half of a bilayer structure. As shown in Fig. 2, the sides of the molecular hexagonal prisms cut across alternate apexes of the crystallographic hexagonal prisms and vice versa: the two microscopic hexagons are rotated 30°. Determining which hexagonal prism orientation coincides with the macroscopic hexagonal prism hinges on location of the crystallographic *a* axis (Fig. 2) in the macroscopic prism (Fig. 1). As indicated

Significance

Ice surface molecular structures determine reactions and interactions on ice. Observation of macroscopic (etch pit) and microscopic (electron backscatter diffraction orientation density function) images definitively shows the molecular-level termination and the layer structure. Identification of the molecular-level structure enables a statistical model that accounts for observation of contrasting growth from the vapor and growth from the liquid. At the solid–vapor interface, the surface is dominated by primary prism and basal faces. In contrast, the secondary prism face dominates at the solid–liquid interface. A statistical model suggests a basis for this contrast: growth at the liquid–solid interface is enthalpically driven, whereas poor thermal transport in the vapor suppresses growth of the secondary prism face.

Author contributions: A.B., P.J.B., and M.J.S. designed research; A.B., K.H., I.B., P.J.B., C.P.D., and M.J.S. performed research; K.H., I.B., E.H.G.B., P.J.B., M.B., C.P.D., M.D.M., and M.J.S. analyzed data; and M.J.S. wrote the paper.

The authors declare no conflict of interest.

This article is a PNAS Direct Submission.

[1]To whom correspondence should be addressed. Email: mary.shultz@tufts.edu.

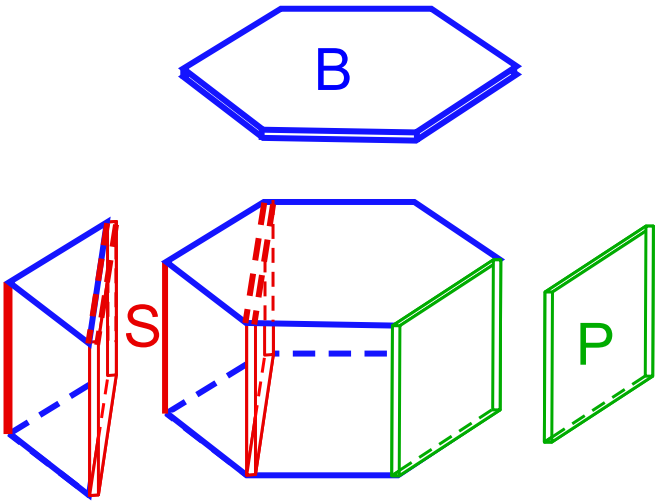

Fig. 1. Illustration of the major faces of a hexagonal prism. B, basal face; P, primary prism face; S, secondary prism face.

above, the answer impacts the molecular-level configuration of the macroscopic prism faces; therefore, is increasingly relevant.

Scattering techniques using X-rays, neutrons, or electrons are ideally suited to locate the crystallographic *a* axis. Mizuno (13) used X-ray scattering to connect the crystallographic axes with those of hoar ice crystals, concluding that crystallographic and hexagonal plate axes coincide. However, later, Mizuno and Wakahama (14) showed that, although the *c* axis of a single-crystal drop frozen on the basal face of a single-crystal substrate coincides with the substrate *c* axis, the *a* axis of the drop is rotated 8° relative to the underlying lattice. Axis rotation along with distorted hexagons observed in the original work (13) suggest that investigation with newer tools is in order. Today, a variety of experimental techniques are available to study the molecular-level structure of ice crystals and their surfaces (15). In particular, high-throughput instruments using the X-ray Laue technique in transmission geometry have been established to generate microscopic orientation maps of sliced polycrystalline samples in 2D; hexagonal crystallites are not observed (16). Recently, X-ray diffraction data from single-crystal ice were used to connect macroscopic and microscopic structures. The scattering data consisting of tables with Euler angles (e.g., supporting information of ref. 17) are less accessible than the electron backscatter diffraction (EBSD) orientation density function (ODF) data reported here. Additionally, charge on the electron ensures that EBSD samples the surface at a micrometer depth, comparable with etch pit images. Thus, EBSD data and etch pit images originate from the same location, compelling connecting the two hexagonal prisms.

Connecting the molecular-level structure and the macroscopic observed shape identifies the layer structure and termination for the two prism faces. Results show that the macroscopic hexagonal points coincide with the crystallographic *a* axes. Hence, the macroscopic primary prism face is the $\{10\bar{1}0\}$ plane; the secondary prism face is the $\{11\bar{2}0\}$ plane. The connection with structure and termination, in turn, supports a model for the surface energies that accounts for observations of surface growth. At the liquid–solid interface, the secondary prism face is more stable than the primary prism or basal face (18). In contrast, at the solid–vapor interface, the primary prism and basal faces are the dominant faces. The key distinction between growth from the liquid and that from the vapor is thermal conduction; growth at the solid–liquid interface is thermodynamically controlled, whereas that at the solid–vapor interface is kinetically controlled. The molecular-level structure and model are presented in *Discussion*.

Briefly, large single-crystal samples were generated (19) and oriented (20) to expose a selected face: the basal, the primary prism, and the secondary prism faces. All surfaces were etched, and the same surface was indexed with EBSD. Etching (21–23) exposes the macroscopic hexagonal prism; the EBSD ODF data reveal orientation of the crystal lattice with respect to the surface normal—a key capability for connecting the macroscopic and microscopic structures. Because both the macroscopic and microscopic hexagonal prism orientations are related to the same surface plane, their mutual orientation is clearly shown. The data indicate that the hexagonal axes of macroscopic hexagonal prism ice align with those of the crystallographic hexagonal prism.

The next section describes the growth, etching, and EBSD techniques. *Results* shows juxtaposition of the etch pit photomicrograph and EBSD ODF plots from each of three principal ice faces. *Discussion* presents implications for the dangling bond and nearest neighbor configurations of each of the prism faces, including enthalpy and entropy consequences. The primary and secondary prism faces switch from the secondary prism face being more stable at the ice–liquid interface to dominance of the primary face at the ice–vapor interface. *Discussion* presents a basis for this switch.

Experimental Procedures

In this investigation, it is critical to grow relatively large single crystals of ice and cut them such that one of three principal faces is exposed at the surface. Single-crystal ice boules were grown using a modified Bridgeman apparatus described previously (19). This apparatus produces very pure single-crystal boules with smooth sides that aid in crystal alignment. Because of the birefringence of ice, the *c* or optical axis is determined quite accurately ±1° using a crossed polarizer stage (Fig. 3). A basal face is produced by cutting perpendicular to the *c* axis. Orientation of the macroscopic hexagon is determined using Formvar etching. A simple two-axis stage enables cutting any desired face, including the primary prism and secondary prism faces (20). Ice samples were cut to present one of the principal prism faces on the surface of the macroscopic sample and further cut to have a chiral shape, thereby eliminating any confusion concerning orientation.

A field emission gun environmental scanning electron microscope (FEI XL-30) equipped with a Gatan cryotransfer/cooling system (HKL/Nordlys) and software (HKL Channel 5 Flamenco v5) was used for the indexing of all collected electron backscatter patterns (EBSPs) (24–26). Using the environmental mode of the SEM, the SEM chamber was backfilled with 0.6 torr N_2 to enable charge bleed off during indexing. In the SEM, ice samples were held in a copper fixture mounted to the cold stage with the temperature held at −130 °C to prevent sublimation. Raw EBSP data were then post-processed (open source MTEX 4.3.1 running under Matlab R2015) to generate the ODF plots shown in Fig. 4.

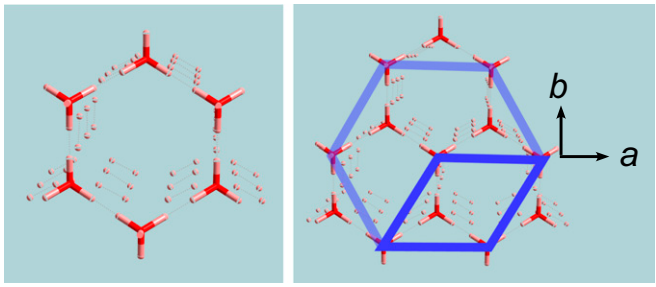

Fig. 2. Top view of the basal face of ice. (*Left*) The chair molecular hexagon—here labeled as the molecular hexagon—defines a hexagonal prism; the prism rectangular faces lack a bilayer structure. (*Right*) The crystallographic unit cell, outlined in dark blue, contains parts of two molecular hexagons. A central water molecule and six nearest neighbors define a hexagonal shape (outlined in light blue)—here labeled as the crystallographic hexagon. The rectangular faces of the hexagonal prism generated from the crystallographic hexagon have a bilayer structure.

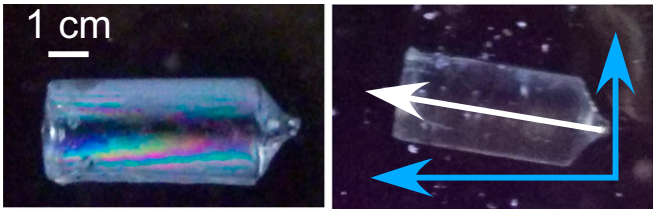

Fig. 3. Photographs of a short single-crystal boule between crossed polarizers viewed along the axis perpendicular to both polarizers. (Polarizer directions are shown schematically with the blue arrows in the right-hand plate.) (*Left*) Rotating the boule on its axis produces a dark "tiger stripe" along the boule length when the optical axis is along the viewing direction. (*Right*) Rotating the boule on its axis (white arrow) by 90° and then rotating perpendicular to the boule axis result in the entire boule going dark. In this orientation, the optical axis is aligned with one of the polarizer directions. Because the optical axis is almost always near perpendicular to the boule axis, it is vertical in the illustrated boule.

Using the flat side and chiral cut, the ice sample was mounted on the copper fixture of the SEM in a known orientation. A thin layer of frost typically accumulated on the ice surface during transfer to the SEM chamber. Frost was removed by increasing the temperature of the cold stage to −60 °C for a short interval of time (1–2 min). Frost asperities are higher energy; thus, they quickly sublimate. During this time interval, surface flatness and quality were monitored with the SEM in secondary electron mode. The sample was then tilted 70° off the horizontal plane of the sample (27) to collect EBSD data. Typically, a resolution of 50 μm is used within a 1-mm^2 sampled area to yield axis orientation data.

Etch pits were produced using Formvar (21). An ice sample several millimeters thick was melt-glued to a microscope slide and placed on the stage of a microscope (polarizing model ML9000; Meiji) located in a −18 °C freezer. A guide was used to reproducibly position the microscope slide and ice sample. The microscope stage was resistively heated to ∼−10 °C. The specimen was examined at 10× until the surface appeared microscopically smooth. The sample was coated with a thin Formvar (2% polyvinyl formal in ethylene chloride) solution. As etch pits developed, they were monitored using a camera (Pixelink PL-A662); images were captured digitally. Orientation of the macroscopic specimen was recorded to connect to orientation in the SEM.

Etch pits were viewed from directly over the sample; vertical and horizontal directions were referenced to the flat sides of the ice specimen that was fixed parallel to the long side of the microscope slide. Image orientation was determined to ±1° by imaging microtome striations (oriented vertically on the specimen) that result from flattening the surface before self-annealing the sample. Because asperities on the surface are high energy, self-annealing in a vapor-saturated atmosphere nets a microscopically flat surface. Applying Formvar is thought (21, 23) to create pinholes in the thin polymer coating, allowing ice to vaporize and revealing the macroscopic structure. Pits grow but maintain the same shape with time. Images were typically on the order of tens of micrometers in Fig. 4, *Right*.

Results

Fig. 4 contains photomicrographs of the etch pits (Fig. 4, *Right*) and ODF plots (Fig. 4, *Left*) of the EBSD data. The chiral shape of the specimen ensures that both etch pit and EBSD ODF data are referenced to the same macroscopic orientation; hence, macroscopic etch pit orientations can be directly compared with the crystallographic EBSD data.

EBSD data were postprocessed to produce ODF—2D projection of the half sphere—plots (Fig. 5) showing the maxima of the observed indexed crystallographic orientation. Because the sample indexed with EBSD is a single crystal, ODF data result in "hot spots" caused by the axis plane projection spots being tightly clustered. The images in column 1 of Fig. 4, *Left* show that all surfaces are flat single crystals. Fig. 4, *Top Left* shows that the *c* axis is near perpendicular (slightly tilted toward the 1:00 AM/PM direction); Fig. 4, *Right* also shows only a slight deviation from perpendicular as evidenced by the central dark spot being slightly off the center of the hexagon.

Similarly, the images in column 1 in Fig. 4, *Middle Left* and *Bottom Left* show that the *c* axis is nearly in the surface plane. The two ends are nearly symmetric; Fig. 4, *Middle Left* shows a little more intensity at the 4:00 AM/PM position than at the 10:00 AM/PM position, whereas Fig. 4, *Bottom Left* shows more intensity at 7:00 AM/PM with respect to 1:00 AM/PM; the *c* axis is slightly tilted upward at the 4:00 and 7:00 AM/PM positions in Fig. 4, *Middle Left* and *Bottom Left*, respectively. The companion etch pits in Fig. 4, *Middle Right* and *Bottom Right* show a corresponding slight deviation from a rectangular outline.

The power of this work is in correlating the hexagonal shape of the EBSD ODF images with the etch pit profiles. Accordingly, the etch pit truncated hexagonal prism profiles are traced, magnified, and overlaid on the ODF plots. Fig. 4, *Top Left* shows the basal face. The sides of the hexagonal etch pit—the primary prism sides—are perpendicular to the crystallographic *b* axes (Fig. 2, *Right*). The crystallographic *a* axes align with the etch pit hexagonal points. Note that, because of hexagonal symmetry, the *a* and *b* axes are only separated by 30°. Thus, careful sample alignment for EBSD ODF and etch pit sampling is essential.

Data from the primary and secondary prism face samples, shown in Fig. 4, *Middle Left* and *Bottom Left*, are consistent with the conclusion drawn from the basal face. The *c*-axis orientation in the ODF plots (column 1 of Fig. 4, *Left*) and the etch pit profiles (column 3 of Fig. 4, *Left*) are aligned, confirming that relative sample orientation is maintained between etch pit profile sampling and placement in the SEM chamber. The truncated hexagonal prism for a primary face sample (Fig. 4, *Middle Left*) consists of submerged rectangular sides; it appears as a flat-bottomed boat. Consistent with the basal data, the *b* axis is orthogonal to the rectangular sides. The truncated hexagonal prism for a secondary face sample (Fig. 4, *Bottom Left*) consists of the submerged hexagonal points; it appears as a V-bottomed boat. The crystallographic *a* axis aligns with a vector drawn from the center through the hexagonal point.

The combined EBSD ODF data and etch pit profiles from all three major faces support the same conclusion: the macroscopic hexagonal structure observed in snowflakes, etch pits, hoarfrost dendrites, and Tyndall flowers coincides with the crystallographic hexagonal prism.

Discussion

Ice is a fundamentally important hydrogen-bonded solid. Chemically, ice is the simplest example of a hydrogen-bonded material. The multiple configurations of two donors and two acceptors about a tetrahedral oxygen atom result in considerable configurational flexibility—most famously netting the residual entropy at 0 K (28). Because of dangling valences, the ice surface has even greater configurational flexibility. Probing and understanding the surface configuration, including responses to interactions with impinging molecules, are keys to unraveling the impact of ice on environmental and biological systems. Understanding ice surfaces in these settings begins with a picture of the ideal termination.

The bulk crystalline structure of ice, known since controversies were resolved in 1929 (29), consists of a rhombohedral prism unit cell (Fig. 2). Tessellating a 2D plane with the rhombohedral faces generates a hexagonal structure—referred to as the crystallographic hexagon—consisting of the six next nearest neighbors of a central water molecule. Nearest neighbor water molecules form a chair hexagon structure—referred to as the molecular hexagon. Literature reports (2–4, 13) connecting either of these hexagonal structures with hexagonal prisms observed in snowflakes, hoarfrost dendrites, Tyndall flowers, or etch pits are based on the assumption that dendrites grow along low crystallographic index directions, exposing low index faces. However, there are numerous counterexamples to this assumption: face-centered cubic crystals form {111} faces rather than lower index {101} or even lower index {100} faces (6, 30). Indeed, the

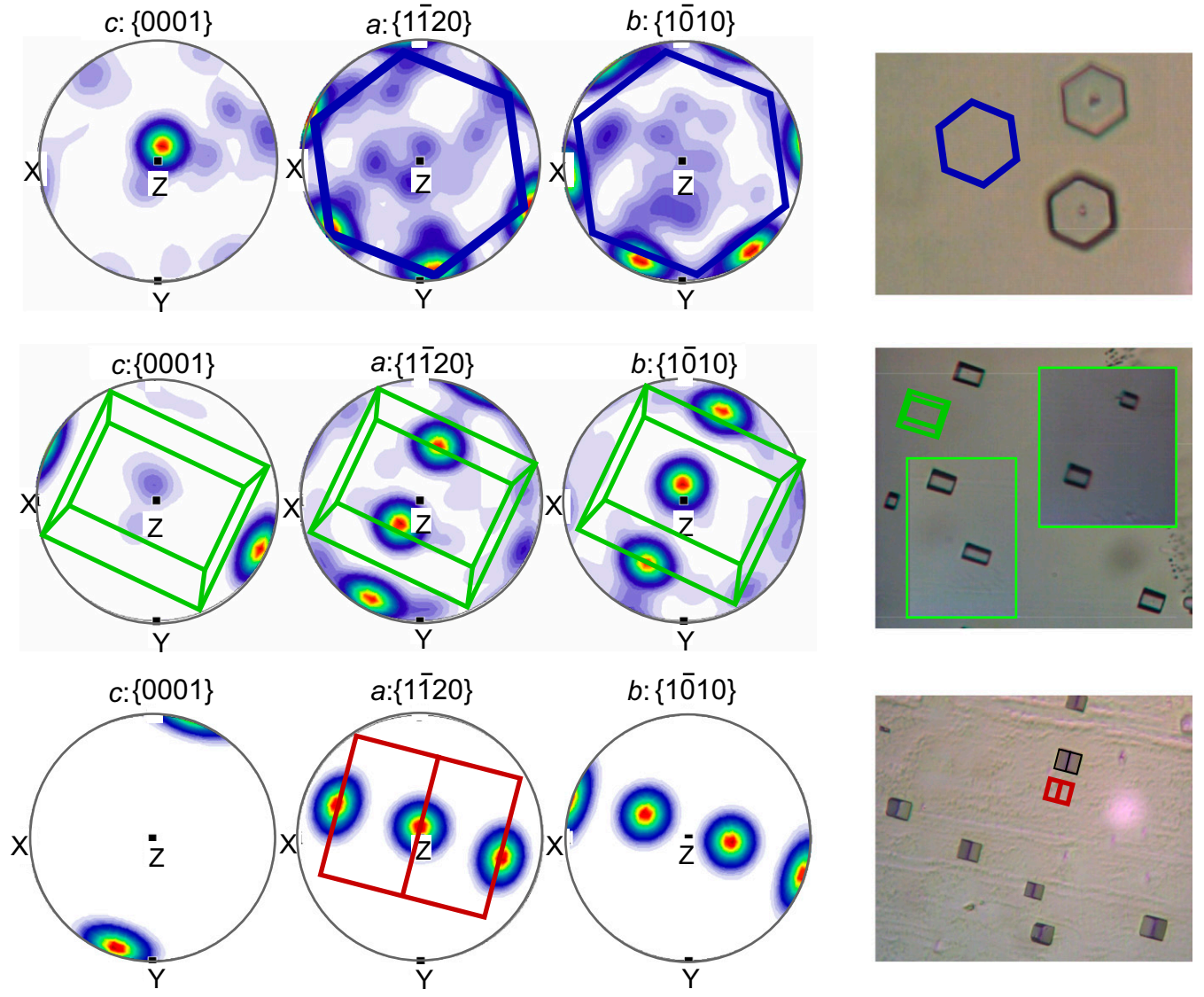

Fig. 4. (*Left*) ODF pole plot and (*Right*) etch pits of the same crystal surfaces. Alignment of the etched and EBSD imaged samples is ensured by consistent orientation of the macroscopic sample reference edges. (*Top Left*) The ODF pole plot in column 1 indicates that the *c* axis is nearly perpendicular to the surface: a near-perfect basal face. The hexagonal etch pit in *Top Right* is outlined, magnified, and overlaid on the ODF plot. The ODF plots in columns 2 and 3 in *Top Left* indicate that the crystallographic *a* axes {11$\bar{2}$ 0} align with the etch pit hexagonal points; the *b* axes {10$\bar{1}$ 0} are orthogonal to the rectangular sides. (*Middle Left*) The ODF pole plot in column 1 indicates that the *c* axis is nearly parallel to the surface: an excellent prism cut. The flat-bottomed etch pit in *Middle Right* is outlined in green, magnified, and overlaid on the ODF plot in column 3 in *Middle Left*. The crystallographic *b* axis is perpendicular to the etch pit rectangular face. (This surface produced few etch pits, and therefore, the pit image is a composite of pits from different spots on the surface.) (*Bottom Left*) The ODF pole plot in column 1 indicates that the *c* axis is nearly parallel to the surface. The V-bottomed etch pit in *Bottom Right* is outlined in red, magnified, and overlaid on the ODF plot. The crystallographic *a* axes {11$\bar{2}$ 0} pass through the hexagonal points. All panels in *Left* definitely show that the crystallographic *a* axes correspond to apices of the hexagonal etch pits; the *b* axes are orthogonal to the rectangular sides.

exposed faces are determined by energy (6–8, 31) or kinetics, not crystallographic indices.

The molecular structure of the ice basal face is independent of which hexagon determines the macroscopic shape, but that is not so for the prism faces. As the prism faces come under greater scrutiny, determining which microscopic hexagon connects to the macroscopic structure becomes increasingly important. Macroscopically, the rectangular sides of the hexagonal prism are termed primary prism faces; cuts across alternate hexagonal points are termed secondary prism faces. The molecular-level termination of these prism faces depends on which microscopic hexagon is connected with the macroscopic one. As shown in Fig. 2, rectangular sides of the molecular hexagon, the $\{11\bar{2}0\}$ faces, lack a bilayer structure; rectangular sides of the crystallographic hexagon, the $\{10\bar{1}0\}$ faces, form a bilayer structure. Furthermore (Fig. 6), the $\{10\bar{1}0\}$ faces feature pairs of hydrogen-bonded water molecules, whereas the $\{11\bar{2}0\}$ faces consist of hydrogen-bonded water molecule chains. Interactions, mobility, and the fate of impinging molecules likely depend strongly on which molecular motif is encountered.

This work presents a direct connection between the macroscopic and microscopic hexagonal prisms. The macroscopic prism is generated via etching producing a truncated, partially submerged hexagonal prism. The same surface is indexed with EBSD, thereby revealing the crystallographic axes. Producing both images on the same surface enables a direct connection, showing that the macroscopic hexagonal prism coincides with the crystallographic prism. Consequently, the macroscopic primary

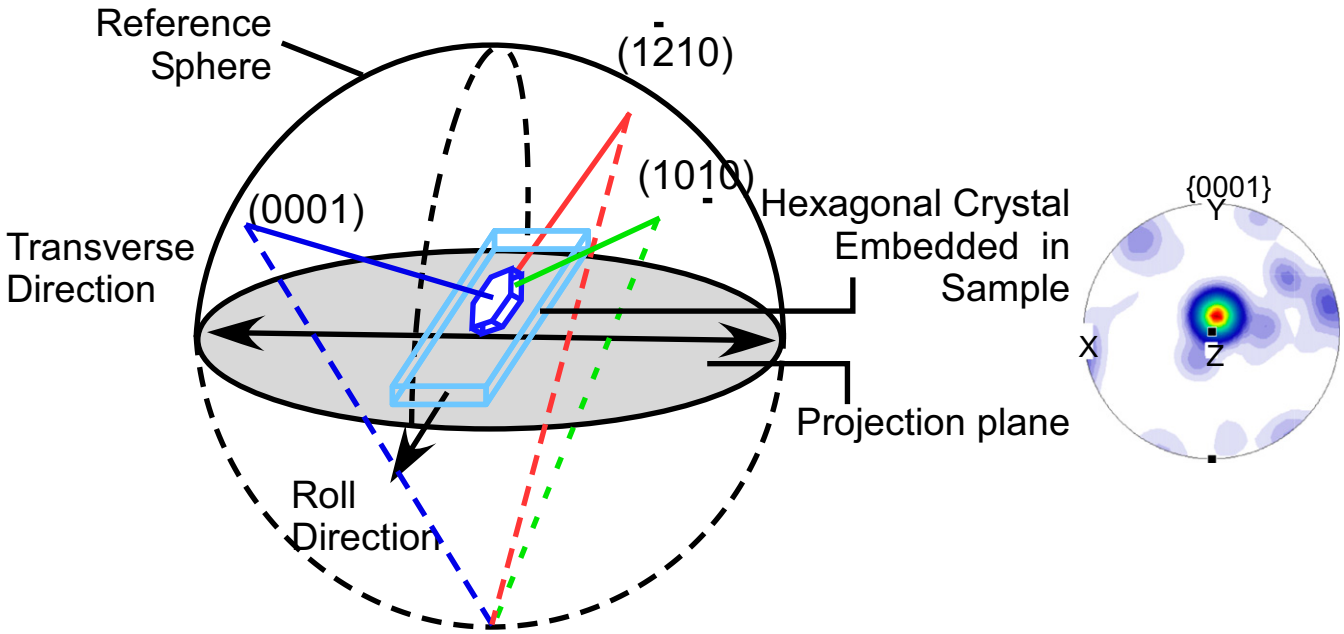

Fig. 5. Illustration of ODF plot creation. Imagine the sample enclosed in a sphere. Scattering corresponding to each of the three axes: *a*–*c* penetrate the sphere surface. Penetration points from the multiple sampled points (nearly 400 in the data shown in Fig. 4) are connected with a straight line to the South Pole. The point where each of these lines passes through the equatorial plane generates a scatter plot in the plane. The ODF is a contour plot of the density; high density is indicated with red, low density is indicated with blue, and very low density is indicated with white. A polycrystalline sample produces multiple hot spots; a single-crystal sample produces a few very hot spots. In this example, the *c*-axis points are tightly clustered, indicating that *c* axes from all sampled spots are tightly clustered.

prism face is the $\{10\bar{1}0\}$ crystallographic face, is terminated with hydrogen-bonded pairs, and consists of a bilayer structure. Conversely, the macroscopic secondary prism face is the $\{11\bar{2}0\}$ crystallographic face, is terminated with hydrogen-bonded water molecule chains, and lacks a bilayer structure.

The differing terminations affect both components—the enthalpy and the configurational entropy—of the surface Gibbs free energy. The following is a simple model illustrating the consequences of these differences (18, 32). Enthalpy for water molecule attachment to the top layer is proportional to the dangling valence density, generating 5.9 $\mu J \cdot cm^{-2}$ for the primary prism face compared with 6.9 $\mu J \cdot cm^{-2}$ for the secondary prism face. Surface entropy of each of these faces is estimated relative to the residual entropy of bulk ice: ln(3/2) (28). Relative to the bulk, the entropy of the faces differs because of differing interlayer attachment. The secondary prism face has a structure consisting of chains of hydrogen-bonded water molecules that bridge chains in the next monolayer (Fig. 6). To satisfy the ice rules (28, 33), top-layer chains must complement dangling valences from the accepting layer: *d*-H to *d*-O and vice versa. Each link has a probability of 1/2 of being complementary, netting a configurational entropy, *S*, for the secondary prism face of 1.10 $\mu J \cdot cm^{-2}$ at 0 °C. The primary prism face consists of pairs of water molecules offset from and bridging four pairs in the lower half bilayer (Fig. 6). The pair–bilayer structure nets greater configurational flexibility and hence, higher configurational entropy for the primary prism face: 1.23 $\mu J \cdot cm^{-2}$ at 0 °C. Experimental observation that the secondary prism face edges out the primary prism face for growth at the liquid–solid interface (27) indicates that the free energies are closely matched but that the secondary prism face has slightly lower energy than the primary prism face; the greater exothermicity tips the balance in favor of the secondary prism face. Dominance of the secondary prism face at the solid–liquid interface contrasts with growth at the solid–vapor interface, where the primary prism face is observed along with the basal face cap. Possibly, poor thermal conductivity of the vapor results in the secondary face self-melting, thus inhibiting its growth. Greater thermal conductivity of the liquid dissipates heat released, maintains equilibrium, and tilts the balance in favor of the secondary prism face.

The literature is inconsistent concerning ice surface free energies. Experimental measurements are challenging, but recent measurements—both attachment kinetics (34) and competitive growth (18)—consistently show that the prism faces are more stable than the basal face at the normal freezing point. In contrast, theoretical results (12, 35, 36) consistently calculate a lower energy for the basal face. Note that theoretical models also show a layered structure with hexagonal ice alternating with cubic ice. Such alternation is not seen in the experimental results. The molecular configuration of the faces supports the theoretical conclusion that entropy is key (35). We speculate that the boat conformation hexagons, found on the prism faces of hexagonal ice but not present in cubic ice, may provide insight into disagreement between theory and experiment. Because surface tension is known to impact properties, such as wetting, adsorption, and reaction energetics, identifying the molecular-level structure of the faces is an important step.

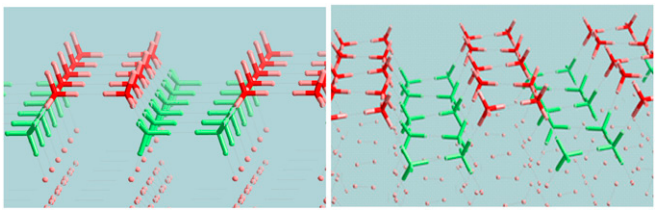

Fig. 6. (*Left*) The ice $\{10\bar{1}0\}$ face is terminated with pairs of water molecules and has a bilayer structure. (*Right*) The $\{11\bar{2}0\}$ face is terminated with hydrogen-bonded chains of water molecules and lacks a bilayer structure.

Summary

This work takes advantage of large single-crystal ice samples to generate both macroscopic and microscopic measurements on the same surface, enabling a direct connection. Macroscopic hexagonal prisms are revealed using a Formvar etching technique (21). Crystallographic axes are measured using EBSD indexing and ODF plots (27). Tracing the etch pit profile and overlaying it on the ODF plot for each of three major ice faces definitively reveal that the etch pit hexagonal prism coincides with the crystallographic prism.

Thus, the previous literature conclusion (2–4, 13, 17) that the macroscopic hexagon coincides with the crystallographic hexagon is verified. The visually compelling correlation between EBSD ODF plots and surface etch images presented here cements this connection. The fundamental connection between the macroscopic and microscopic is face energies; observation of secondary prism and not primary prism faces at the solid–liquid interface indicates that the energy of the $\{11\bar{2}0\}$ face is slightly lower than that of the $\{10\bar{1}0\}$ face. Dominance is reversed at the solid–vapor interface, which has been attributed to a kinetic heat conduction effect. The direct experimental connection presented here definitively links the macroscopic structure to the molecular-level termination and bilayer structure, enabling the above interpretation.

ACKNOWLEDGMENTS. E.H.G.B., M.B., and M.D.M. thank Jenée Cyran, Tanja Kling, Alejandra Sánchez, and Marc-Jan van Zadel for helpful discussion. P.J.B. and M.J.S. acknowledge partial support from US National Science Foundation Grants CHE1449643 and CHE1565772.

1. Kepler J (1611) *On the Six-Cornered Snowflake (Godfrey Tampach, Drankfort on Main, 1611)*, trans Hardie C (1966) (Oxford Univ Press, London).
2. Bader H (1939) *Der Schnee Und Seine Metamorphose (Beitrage zur Geologie der Schweiz*, Translation 14) (Kümmerly & Frey, Bern, Switzerland).
3. Nakaya U (1956) *Research Paper 13: Properties of Single Crystal Ice, Revealed by Internal Melting* (US Army Corps of Engineers, Wilmette, IL).
4. Bader H (1950) The significance of air bubbles in glacier ice. *J Glaciol* 1:443–451.
5. Wulff G (1901) On the question of speed of growth and dissolution of crystal surfaces. *Z Kryst Mineral* 34:449–530.
6. Sehgal RM, Maroudas D (2015) Equilibrium shape of colloidal crystals. *Langmuir* 31: 11428–11437.
7. Degawa M, Szalma RF, Williams ED (2005) Nano-scale equilibrium crystal shapes. *Surf Sci* 583:126–138.
8. Barnard AS, Zapol P (2004) A model for the phase stability of arbitrary nanoparticles as a function of size and shape. *J Chem Phys* 121:4276–4283.
9. Libbrecht KG (2004) On the equilibrium shape of an ice crystal. arXiv:1205.1452v1.
10. Libbrecht KG (2014) Toward a comprehensive model of snow crystal growth: 3. The correspondence between ice growth from water vapor and ice growth from liquid water. arXiv:1407.0740.
11. Libbrecht KG (2013) Toward a comprehensive model of snow crystal growth dynamics: 2. Structure dependent attachment kinetics near -5 C. arXiv:1302.1231.
12. Handel R, Davidchack RL, Anwar J, Brukhno A (2008) Direct calculation of solid-liquid interfacial free energy for molecular systems: TIP4P ice-water interface. *Phys Rev Lett* 100:036104.
13. Mizuno Y (1978) Studies of crystal imperfections in ice with reference to the growth process by the use of X-ray diffraction topography and divergent laue method. *J Glaciol* 21:409–418.
14. Mizuno Y, Wakahama G (1983) Structure and orientation of frozen droplets on ice surfaces. *J Phys Chem* 87:4161–4167.
15. Miyamoto A, Weikusat I, Hondoh T (2011) Instruments and methods complete determination of ice crystal orientation using Laue X-ray diffraction method. *J Glaciol* 57:103–110.
16. Mori Y, Hondoh T, Higashi A (1985) Development of an automatic ice fabric analyzer. *Ann Glaciol* 6:281–283.
17. Sánchez MA, et al. (2017) Experimental and theoretical evidence for bilayer-by-bilayer surface melting of crystalline ice. *Proc Natl Acad Sci USA* 114:227–232.
18. Shultz MJ, Bisson PJ, Brumberg A (2014) Best face forward: Crystal-face competition at the ice-water interface. *J Phys Chem B* 118:7972–7980.
19. Bisson P, Groenzin H, Barnett IL, Shultz MJ (2016) High yield, single crystal ice via the Bridgman method. *Rev Sci Instrum* 87:034103.
20. Shultz MJ, Brumberg A, Bisson PJ, Shultz R (2015) Producing desired ice faces. *Proc Natl Acad Sci USA* 112:E6096–E6100.
21. Higuchi K (1958) The etching of ice crystals. *Acta Metall* 6:636–642.
22. Higuchi K (1957) A new method for recording the grain-structure of ice. *J Glaciol* 3: 131–132.
23. Matsuda M (1979) Instruments and methods: Determination of *a*-axis orientations of polycrystalline ice. *J Glaciol* 22:165–169.
24. Iliescu D, Baker I, Chang H (2004) Determining the orientations of ice crystals using electron backscatter patterns. *Microsc Res Tech* 63:183–187.
25. Obbard R, Baker I, Sieg K (2006) Using electron backscatter diffraction patterns to examine recrystallization in polar ice sheets. *J Glaciol* 52:546–557.
26. Baker I, Sieg K, Spaulding N, Meese D (2007) *Advanced Electron Microscopy Techniques for Studying Ice and Firn Cores* (US Geological Survey and the National Academies, Reston, VA), Extended Abs 185.
27. Prior DJ, et al. (2015) Making EBSD on water ice routine. *J Microsc* 259:237–256.
28. Pauling L (1935) The structure and entropy of ice and other crystals with some randomness of atomic arrangement. *J Am Chem Soc* 57:2680–2684.
29. Barnes WH (1929) The crystal structure of ice between 0 degrees C and -183 degrees C. *Proc R Soc Lond A Math Phys Sci* 125:670–693.
30. Saito Y (1981) Wulff polyhedra derived from Morse potentials and crystal habits of Bcc and Fcc metal particles. *J Cryst Growth* 53:273–279.
31. Ringe E, Van Duyne RP, Marks LD (2011) Wulff construction for alloy nanoparticles. *Nano Lett* 11:3399–3403.
32. Shultz MJ, Bisson PJ, Brumberg A (2016) Correction to "best face forward: Crystal-face competition at the ice-water interface." *J Phys Chem B* 120:10420.
33. Bernal JD, Fowler RH (1933) A theory of water and ionic solution, with particular reference to hydrogen and hydroxyl ions. *J Chem Phys* 1:515–548.
34. Libbrecht KG, Rickerby ME (2013) Measurements of surface attachment kinetics for faceted ice crystal growth. *J Cryst Growth* 377:1–8.
35. Espinosa JR, Veg C, Sanz E (2016) Ice–water interfacial free energy for the Tip4p, Tip4p/2005, Tip4p/Ice, and Mw models as obtained from the mold integration technique. *J Phys Chem C Nanomater Interfaces* 120:8068–8075.
36. Ambler M, Vorselaars B, Allen MP, Quigley D (2017) Solid-liquid interfacial free energy of ice Ih, ice Ic, and ice 0 within a mono-atomic model of water via the capillary wave method. *J Chem Phys* 146:074701.